RSC Advances

ROYAL SOCIETY OF CHEMISTRY

www.rsc.org/advances

$MnFe_2O_4$-Fe_3O_4 Core-Shell Nanoparticles as Potential Contrast Agent for Magnetic Resonance Imaging

N Venkatesha[1], Shivanad M Pudakalakatti[2], Yasrib Qurishi[3], Hanudatta S. Atreya[2], Chandan Srivastava[1*]

[1]Department of Materials Engineering, Indian Institute of Science, Bangalore, India
[2]NMR Research Centre, Indian Institute of Science, Bangalore, India
[3]Department of Molecular Reproduction, Development and Genetics, Indian Institute of Science, Bangalore, India

*Corresponding Author: Email: csrivastava@materials.iisc.ernet.in
Phone: 91-080-22932834
Fax: 91-080-2360 0472

Abstract

In recent years, magnetic core-shell nanoparticles have received widespread attention due to their unique properties that can be used for various applications. We introduce here a magnetic core-shell nanoparticle system for potential application as a contrast agent in magnetic resonance imaging (MRI). $MnFe_2O_4$-Fe_3O_4 core-shell nanoparticles were synthesized by the wet-chemical synthesis method. Detailed structural and compositional charaterization confirmed the formation of core-shell microstructure for the nanoparticles. Magnetic charaterization revealed the superparamagnetic nature of the as-synthesized core-shell nanoparticles. Average size and saturation magnetization values obtained for the as-synthesized core-shell nanoparticle were 12.5 nm and 69.34 emu/g respectively. Transverse relaxivity value of the water protons obtained in presence of core-shell nanoparticles was 184.1 $mM^{-1}s^{-1}$. To investigate the effect of core-shell geometry towards enhancing the relaxivity value, transverse relaxivity values were also obtained in the presence of separately synthesized single phase Fe_3O_4 and $MnFe_2O_4$ nanoparticles. Average size and saturation magnetization values for the as-synthesized Fe_3O_4 nanoparticle were 12 nm and 65.8 emu/g respectively. Average size and the saturation magnetization values for the

$MnFe_2O_4$ nanoparticle were 9 nm and 61.5 emu/g respectively. Transverse relaxivity value obtained in the presence of single phase Fe_3O_4 and $MnFe_2O_4$ nanoparticles was 96.6 and 83.2 $mM^{-1}s^{-1}$ respectively. All the nanoparticles (core-shell and single phase) were coated with chitosan by a surfactant exchange reaction before determining the relaxivity values. For similar nanoparticle sizes and saturation magnetization values, the highest value of transverse relaxivity in the case of core-shell nanoparticles clearly illustrated that the difference in the magnetic nature of the core and shell phases in the core-shell nanoparticles creates greater magnetic inhomogeneity in the surrounding medium yielding high value of proton relaxivity. The $MnFe_2O_4$-Fe_3O_4 core-shell nanoparticles exhibited extremely low toxicity towards the MCF-7 cell line. Taken together, this opens up new avenues for the use of core-shell nanoparticles in MRI.

Keywords: Magnetic Resonance Imaging, core-shell nanoparticles, contrast agent.

1. Introduction

Multi-phase nanoparticles have been a subject of intensive investigations lately due to their unique and tunable properties which originate primarily from the synergistic response of the co-existing phases to a stimulus.[1,2] Altering the volume fraction of the phases and/or engineering their mutual geometrical arrangement therefore can be used to derive emergent and tune monotonically varying functionalities.[3] Among the multiphase microstructures, core-shell geometry is the one that has been most widely synthesized and investigated.[4] Synthesis of core-shell nanoparticles typically involves initial synthesis of seeds nanoparticles that forms the core. These seeds are then dispersed in a reaction solution where they provide the heterogeneous surface for nucleation and growth of the phase that forms the shell of the core-shell geometry.[5–7]

Recently, magnetic core-shell nanoparticles containing hard and soft magnetic phases have received wide attention due to exchange coupling between the magnetic phases which yields unique properties that can be technologically exploited.[8–11] For example, exchange coupling in ferrite-ferrite core-shell nanoparticles has been exploited for localized heating and killing of cancer cells.[10] Application of core-shell magnetic nanoparticles as hyperthermia agents is due to a phenomenon known as specific loss power (SLP). SLP is the ability of a system to generate heat when exposed to an electromagnetic field.[12,13] Core-shell nanoparticles exhibit significantly higher SLP when compared to the SLP exhibited by single phase nanoparticles. The enhancement in the SLP value is essentially due to the interfacial exchange interaction between magnetic phases in core-shell geometry.[10]

In this paper, we introduce $MnFe_2O_4$-Fe_3O_4 Core-Shell Nanoparticles system for application as a potential contrast agent material in MRI. MRI is now a widely used imaging technique in medical diagnosis.[14] Use of contrast agent materials in MRI is essential for

enhancing the probe sensitivity of the MRI technique.[15-17] One of the most widely explored materials for use as contrast agent in MRI is magnetic nanoparticles and nanoparticle based systems[15-20]. The candidate system chosen for this study is $MnFe_2O_4$-Fe_3O_4 core-shell nanoparticles**.** It should be noted that apart from widely investigated Fe_3O_4 nanoparticles for bio-medical imaging, the potential of $MnFe_2O_4$ nanoparticles for use as MRI contrast agent has been well established by the researchers[21,22]. It has been shown that the $MnFe_2O_4$-Fe_3O_4 core-shell nanoparticles exhibit a very high value of SLP[10]. This study exploits the fact that the differences in the magnetocrystalline anisotropy between the two magnetic phases in the core-shell nanoparticle induces relatively greater magnetic inhomogeneties in the vicinity of these core-shell nanoparticles when compared to the extent of inhomogeneity induced by single phase nanoparticles.[23,24] Greater magnetic inhomogeneity can induce faster dephasing of the magnetic moments thus significantly reducing the T_2 relaxation time and enhancing the transverse relaxivity of the water protons present in the medium surrounding the core-shell nanoparticles. Core-shell nanoparticles exhibiting significantly high value of SLP and proton relaxivity can be used both for imaging the cancer cells and destroying it using localized heating.

2. Experimental

2.1 Synthesis of $MnFe_2O_4$-Fe_3O_4 core-shell system

In the present work, a two step methodology was used to synthesize the $MnFe_2O_4$-Fe_3O_4 core-shell nanoparticles. In the first stage, $MnFe_2O_4$ seed nanoparticles were synthesized and in the second stage Fe_3O_4 phase was grown over the seeds to produce $MnFe_2O_4$-Fe_3O_4 core-shell nanoparticles.

To synthesize $MnFe_2O_4$ nanoparticles, $Mn(acac)_2$ (1 mmol), $Fe(acac)_3$ (2 mmol), 1,2-hexadecanediol (5 mmol), oleic acid (6 mmol), and oleylamine (6 mmol) and diphenyl ether (20

mL) were mixed in a three neck round bottom flask fitted with a magnetic stirrer and a reflux condenser. This reaction mixture was heated to 150 ˚C and kept at this temperature for 30 min. After 30 min, temperature of the reaction mixture was raised to ~250 ˚C and refluxed for 30 min. The nanoparticle synthesis reaction occurred in argon atmosphere. After reflux, the black colored mixture containing precipitated nanoparticles was cooled down to room temperature. 40 mL of ethanol was then added into the nanoparticle dispersion to sediment the nanoparticles which were subsequently isolated by centrifugation.

To synthesize $MnFe_2O_4$-Fe_3O_4 core-shell nanoparticles, 40 mg of $MnFe_2O_4$ nanoparticles were dispersed in 20 mL of hexane by sonication. Into this solution, benzyl ether (20 mL), $Fe(acac)_3$ (3 mmol), oleic acid (6 mmol), oleylamine (6 mmol) and 1,2-hexadecanediol (5 mmol) were added. This reaction mixture was then poured into a three neck round bottom flask fitted with a magnetic stirrer and a reflux condenser. The reaction mixture was heated to 100 ˚C and kept at this temperature for 1 h to evaporate away the hexane. Temperature of the reaction mixture was then raised to 200 ˚C and was kept at this temperature for 60 min. After this, the temperature of the reaction mixture was raised to 290 ˚C and was kept at this temperature for 60 min. After 60 min, the reaction mixture containing nanoparticles was allowed to cool down to the room temperature. 40 mL of ethanol was added into the reaction mixture to sediment the nanoparticles which were isolated by centrifugation. The core-shell nanoparticles obtained were then separated by centrifugation (8000 rpm, 10 min).

2.2 Synthesis of 9 nm $MnFe_2O_4$ nanoparticles

To synthesize $MnFe_2O_4$ nanoparticles, $Mn(acac)_2$ (1 mmol), $Fe(acac)_3$ (2 mmol), 1,2-hexadecanediol (5 mmol), oleic acid (6 mmol), and oleylamine (6 mmol) and benzyl ether (10 mL) were mixed and magnetically stirred under the flow of Argon. This reaction mixture was

heated to 150 ˚C for 30 min. After this, the temperature of the reaction mixture was raised to 290 ˚C (the reflux temperature) and refluxed for 60 min. After 60 min, the reaction mixture containing precipitated nanoparticles was allowed to cool down to the room temperature. The synthesis reaction was conducted under argon atmosphere. At the room temperature, 40 mL of ethanol was added into the reaction mixture to sediment the nanoparticles which were subsequently isolated by centrifugation.

2.3 Synthesis of 12nm Fe_3O_4 nanoparticles

To synthesize Fe_3O_4 nanoparticles, $Fe(acac)_3$ (3 mmol), 1,2-hexadecanediol (5 mmol), oleic acid (6 mmol), and oleylamine (6 mmol) and benzyl ether (10 mL) were mixed and magnetically stirred under the flow of Argon . This reaction mixture was heated to 150 ˚C for 30 min. After which the temperature of the reaction mixture was raised to 290 ˚C (reaction mixture reflux temperature) and refluxed for 60 min. After 60 min, the reaction mixture containing precipitated nanoparticles was allowed to cool down to the room temperature. At room temperature, 40 mL of ethanol was added into the reaction mixture to sediment the nanoparticles which were subsequently isolated by centrifugation.

2.4 Coating of nanoparticles with chitosan

Uniform dispersion of nanoparticles in water is essential for bio-medical applications. To make the nanoparticles water dispersible, a surfactant exchange reaction was conducted in which oleyl amine and oleic acid on the nanoparticle surface were replaced by chitosan.[24] Chitosan (β-(1-4)-linked D-glucosamine (deacetylated unit) and N-acetyl-D-glucosamine (acetylated unit)) is a biocompatible polymer which has been tested widely for various bio-medical applications.[26] For the ligand exchange reaction, 50 mg of nanoparticles were dispersed in 20 ml of hexane by sonication. A solution was prepared by dissolving DMSA (2,3-dimercaptosuccinic acid) into

DMSO (dimethyl sulfoxide) in 10(w/v) % ratio. Into this solution, the nanoparticle dispersion was added in 1:1 ratio by volume and sonicated for 1 h. Hexane layer containing organic precursors was separated by using separating funnel and DMSA coated water soluble nanoparticles were dispersed in DMSO. The nanoparticles were then washed using DI water and isolated by magnetic separation. Chitosan solution was prepared by dissolving 0.5 g of chitosan in a 2.0 % aqueous acetic acid solution by magnetic stirring for 30 min. 5 mL of this solution was then added into the aqueous dispersion containing DMSA-coated nanoparticles and sonicated for 1 h. During the sonication, chitosan got electrostatically attached to the nanoparticle surface. Into this dispersion, 50 mg of EDC [1-ethyl-3-(3-dimethylaminopropyl) carbodiimide hydrochloride] was then added and sonicated for further 2 hours. EDC reacted with DMSA carboxyl groups on the surface of the nanoparticles to form an amine reactive O-acylisourea intermediate. This intermediate reacted with the amine group of chitosan yielding water stable chitosan coated nanoparticles. Finally, this sample was washed with water followed by magnetic separation.

2.5 Characterization X-ray diffraction (XRD) profiles were obtained from the as-synthesized samples using the X-Pert PAN Analytical machine employing Cu K-alpha radiation source. A 300 keV field emission FEI Tecnai F-30 transmission electron microscope (TEM) was used for obtaining TEM bright field images and selected area electron diffraction (SAD) patterns from as-synthesised samples. Samples for the TEM based analysis were prepared by drop-drying a highly dilute dispersion of the as-synthesised nanoparticles onto an electron transparent carbon coated Cu grid. Magnetic measurement data from the as-synthesized samples was obtained by using the Lakeshore vibrating sample magnetometer (VSM). Mass of the core-shell nanoparticles was determined by thermal gravimetric analysis (TGA) measurement conducted using the TGA

NETZSCN STA 403 PC machine. The concentration of iron in nanoparticle dispersions used in the NMR experiments was calculated by atomic absorption spectroscopy (AAS) technique conducted using the Thermo Electron Corporation M-series machine. X-ray photoelectron spectroscopy (XPS) profiles were obtained from the as-synthesized samples using an AXIS Ultra DLD (KRATOS ANALYTICAL) instrument.

All NMR experiments were performed at 25°C on a Bruker Avance-III NMR spectrometer operating at a ^{1}H resonance frequency of 400 MHz. Samples were dissolved in 95 % $^{2}H_2O$ and 5 % H_2O. The transverse relaxation of water (H_2O) was measured using CPMG/T_2-filter (Carr Purucell Meiboom Gill) NMR experiment.[27] The relaxation delay time 'τ' was varied between 10 ms to 1 s collecting 12 data points to get the decay curve to extract T_2 relaxation time constant. The 16 K complex points were collected with 1.1 s acquisition time and 7000 Hz spectral width. A relaxation delay of 15 s was given between scans.

Cytotoxicity analysis

Cytotoxicity analysis was carrier out to determine the bio-compatibility of the core-shell nanoparticles[28]. Following procedure was adopted.

Cell culture: MCF-7 is a breast cancer cell line isolated in 1970 from a 69-year-old Caucasian woman. Cells were cultured in Dublecco's Modified Eagle's Medium (DMEM) with 2 mM L-glutamine supplemented with 10% fetal bovine serum (FBS), 45 IU ml− 1 penicillin at 37 °C in 5% CO_2.

Preparation of $MnFe_2O_4$-Fe_3O_4 nanoparticle solution: $MnFe_2O_4$-Fe_3O_4 core-shell nanoparticles were prepared in the cell culture media under laminar flow and sterile conditions. Nanoparticles were dispersed uniformly by low speed vortex. The concentrations used for the cytotoxicity assays with $MnFe_2O_4$-Fe_3O_4 core-shell nanoparticles were 100, 50, 25, 12.5 and 6.25 μg/mL.

Throughout this study, microgram per milliliter concentrations have been chosen as the unit of preference as they enable the response to be easily conceptualized in terms of number of particles, surface area and/or number of surface groups.

MTT assay: MTT assay was performed to evaluate the cytotoxicity of the chitosan coated $MnFe_2O_4$-Fe_3O_4 core-shell nanoparticles. 8000 cells/ml/well were seeded at optimum density into each well of a 96-well microtiter plate and exposed to varied concentrations of chitosan coated core-shell nanoparticles. The cells were then incubated with the chitosan coated $MnFe_2O_4$-Fe_3O_4 core-shell nanoparticles for 24 h. 5 mg/mL MTT dye was then added into each well followed by further incubation for 3-4 h. The medium was discarded and the cells were rinsed with PBS and 150 µl of DMSO was added to each well to extract the dye. The MTT formazon crystals formed were metabolically reduced by the mitochondria in viable cells to a colored formazon product. The plates were shaken at 240 rpm for 10 min and absorbance was measured spectrophotometrically in a plate reader at 570 nm. The intensity of the dissolved colored product (percentage viability) was calculated by comparing the absorbance of treated versus untreated.

3. Results and discussion

XRD profiles obtained from $MnFe_2O_4$ seeds and $MnFe_2O_4$-Fe_3O_4 core-shell nanoparticles are shown in Fig. 1. The XRD profiles reveal diffraction peaks corresponding only to the ferrite phase indicating that the both seeds and core-shell nanoparticles have only ferrite phase.[29]

Average size of the seed and core-shell nanoparticles, obtained from the FWHM of the most intense (311) peak and the Scherrer formula[30] was 4.5 and 12 nm respectively. Increase in the average size of the nanoparticles by ~7 nm is due to the coating of the seed $MnFe_2O_4$ nanoparticles by the Fe_3O_4 phase. TEM bright field image of $MnFe_2O_4$ seed nanoparticles is

provided in Fig. 2(a). It can be observed that the first step of the synthesis process has produced nearly spherical nanoparticles. SAD pattern obtained from the seed nanoparticles showing the presence of only ferrite phase is also shown in Fig. 2(a). Average size of the nanoparticles obtained from the summation average of sizes of 500 individual nanoparticles was 4.9 ±0.5 nm. Histogram showing the distribution of seed nanoparticle sizes is provided in Fig. 2(b). TEM bright field image of $MnFe_2O_4$-Fe_3O_4 core-shell nanoparticles is provided in Fig. 2(c). SAD pattern obtained from the nanoparticles showing the presence of only ferrite phase is also shown in Fig. 2(c). Average size of the core-shell nanoparticles obtained from the summation average of sizes of 500 individual nanoparticles was 12.8±1.1 nm. Histogram illustrating the distribution of the core-shell nanoparticle sizes is provided in Fig. 2(d). It can be observed from Fig. 2(c and d) that the synthesis method has produced core-shell nanoparticles with fairly narrow distribution in sizes. Narrow distribution in nanoparticle sizes and presence of negligible number of nanoparticles with sizes ~5 nm clearly reveals that the reaction conditions adopted in the second step of the synthesis process led to uniform coating of the seed nanoparticles to form uniform core-shell nanoparticles. Core-shell geometry of the nanoparticles produced after the second step of the synthesis process was also confirmed by compositional line profile analysis of individual nanoparticles. A representative compositional line scan analysis result is provided in Fig. 2(e and f). Fig. 2(e) shows the STEM-HAADF image of a representative nanoparticle. The red line on the nanoparticle image is the path along which the compositional data was obtained using an electron probe of ~1.5 nm size. The compositional profile (distance vs. counts) obtained for the Mn atoms is provided in Fig. 2(f). An abrupt increase in the EDS signal from the Mn elements in the middle of the nanoparticles shows that the core of the representative core-shell nanoparticles contained the $MnFe_2O_4$ phase.

Core-shell microstructure was also confirmed from the XPS based analysis of the seed and the core-shell nanoparticles produced respectively in the first and second step of the synthesis process. Fig. 3(a-c) respectively shows the XPS spectra of O1s, Mn2p and Fe2p obtained from the seed and core-shell nanoparticles. Fig. 3(d) shows the complete XPS spectrums. The O1s spectrums (in Fig. 3(c)) obtained from both the samples were deconvoluted into three peaks falling in the binding energy range of 526–533 eV. The peak at ~528.5 eV corresponds to the lattice oxygen species O^{2-} whereas the two peaks at the higher binding energy values of ~529.5 and ~530.5 eV correspond respectively to the hydroxyl and carboxyl group of the oleic acid adsorbed on the surface of nanoparticles.[29] In Fig. 3(a), peaks at 641 and 653 eV corresponding respectively to the $Mn2p_{3/2}$ and $Mn2p_{1/2}$ of Mn^{2+} are observed only for the seed nanoparticles.[31] The Mn2p spectrum of the core-shell nanoparticles do not show any peak suggesting the absence of $MnFe_2O_4$ phase on the surface of the core-shell nanoparticles. The Fe2p spectra (Fig. 3(b)) revealed peaks at ~710 and ~723.3 eV with the separation of 13.3 eV indicating the presence of Fe^{3+}. The XPS results thus clearly revealed the formation of $MnFe_2O_4$-Fe_3O_4 core-shell nanoparticles.

Magnetic hysteresis curves obtained from $MnFe_2O_4$ seeds and $MnFe_2O_4$-Fe_3O_4 core-shell nanoparticles are shown in Fig. 4(a). Magnetic hysteresis curves were obtained at the room temperature using an applied field that varied in the range of 0-2 tesla. As observed in Fig. 4(a), the magnetic hysteresis curves from both $MnFe_2O_4$ seeds and $MnFe_2O_4$-Fe_3O_4 core-shell nanoparticles reveal negligible coercivity and no magnetic saturation till 2 tesla applied field. Both these attributes indicate that the as-synthesized seed and core-shell nanoparticles were superparamagnetic in nature. Saturation magnetization value obtained for the seed and the core-shell nanoparticles respectively was 69.34 and 50.75 emu/g. Superparamagnetic nature was also

confirmed from the occurrence of peak in the form of a broad hump in the ZFC curves for both the nanoparticles. ZFC curves are shown in Fig. 4(b). $MnFe_2O_4$ seed nanoparticles exhibit a clear hump in the ZFC curve. Whereas, the core-shell nanoparticles exhibit a broad peak at higher temperature. The shift of the ZFC curve peak was due to the increase in the nanoparticle size. The broadness of the ZFC curve for the case when the distribution between the particle sizes is narrow (as in the present case for core-shell nanoparticles) essentially illustrates interaction between magnetic spins at the $MnFe_2O_4$ and Fe_3O_4 interface.[32]

Transverse relaxivity of water protons in the presence of chitosan-coated $MnFe_2O_4$-Fe_3O_4 core-shell nanoparticles at different concentrations were measured using the NMR spin-echo method[33]. The exponentially decaying curves obtained for all the samples at different concentrations of iron were used to calculate the transverse relaxivity (T_2) values. The decay plots used for calculating the T_2 of water protons in the presence of chitosan coated core shell nanoparticles are provided in Fig. 5(a). The data points were fitted according to the equation[33]

$$M_{xy}(t) = M_{xy}(0)e^{-t/T_2} \quad \textbf{(1)}$$

Where $M_{xy}(t)$ is the magnetization along XY plane at time t and $M_{xy}(0)$ magnetization along X-Y plane at time t=0. Decay curves clearly show that the transverse magnetization curves have strong dependences on the concentration of nanoparticles. $1/T_2$ vs. iron concentration was plotted and r_2 (transverse relaxivity) value was obtained by determining the slope of the line fitted to the data points. The plot used for the calculation of r_2 values for chitosan-coated $MnFe_2O_4$-Fe_3O_4 core-shell nanoparticles is shown in Fig. 5(b). The transverse relaxivity value determined for the $MnFe_2O_4$-Fe_3O_4 core-shell nanoparticles was 184.1 $mM^{-1}s^{-1}$. It should be noted that this value of transverse relaxivity is significantly higher than the reported relaxivity values for single phase ferrite nanoparticles.[34]

To illustrate the effect of exchange coupling towards enhancing the relaxivity value as observed in the present case of $MnFe_2O_4$-Fe_3O_4 core-shell nanoparticles, ~9 nm sized $MnFe_2O_4$ nanoparticles and ~12 nm sized Fe_3O_4 nanoparticles were also synthesized. Procedures used for the synthesis of single phase $MnFe_2O_4$ and Fe_3O_4 nanoparticles used for the comparative study are provided respectively in section 2.2 and 2.3.

XRD profile, TEM bright field image and M-H curve obtained from the as-synthesized $MnFe_2O_4$ nanoparticles are shown in Fig. 6. The XRD profile in Fig. 6(a) reveals diffraction peaks corresponding only to the ferrite phase indicating that the synthesis process produced $MnFe_2O_4$ phase nanoparticles. Size of the nanoparticles obtained from the FWHM of the (311) peak and the Scherrer formula was 9 nm. TEM bright field image and SAD pattern obtained from as-synthesized nanoparticles is shown in Fig. 6(b). TEM bright field image reveals the formation of faceted nanoparticles. The SAD pattern shows diffraction rings corresponding to the $MnFe_2O_4$ phase. The size distribution histogram obtained from the as-synthesized nanoparticles is provided in Fig. 6(c). It can be seen that the nanoparticles are fairly uniform in size. Magnetic hysteresis curve obtained from $MnFe_2O_4$ nanoparticles using an applied magnetic field in the range of 0-2 tesla are shown in Fig. 6(d). The magnetic hysteresis curve shows negligible coercivity and no magnetic saturation. Both these attributes illustrates the superparamagnetic nature of the as-synthesized $MnFe_2O_4$ nanoparticles. Saturation magnetization value obtained from the magnetic hysteresis curve was 61.5 emu/g.

XRD profile, TEM bright field image and M-H curve obtained for Fe_3O_4 nanoparticles are shown in Fig. 7. XRD curve obtained from the as-synthesized nanoparticles is shown in Fig. 7(a). The XRD profile shows diffraction peaks corresponding only to the Fe_3O_4 phase indicating that the synthesis process has produced Fe_3O_4 phase nanoparticles. Average size of the

nanoparticles obtained from the FWHM of the (311) peak and the Scherrer formula was 12 nm. TEM bright field image and SAD pattern obtained from as-synthesized nanoparticles is shown in Fig. 7(b).TEM bright field image reveals the formation of faceted nanoparticles. The SAD pattern shows diffraction rings corresponding to the Fe_3O_4 phase. Size distribution histogram obtained from the as-synthesized Fe_3O_4 nanoparticles is provided in Fig. 7(c). It can be seen that the nanoparticle are fairly uniform in size. Magnetic hysteresis curve obtained from Fe_3O_4 nanoparticles using an applied magnetic field in the range of 0-2 tesla are shown in Fig. 7(d). The magnetic hysteresis curve shows negligible coercivity and no magnetic saturation. Both these attributes illustrate the superparamagnetic nature of the as-synthesized Fe_3O_4 nanoparticles. Saturation magnetization value obtained from the magnetic hysteresis curve was 65.8 emu/g.

Transverse relaxivity of water protons in the presence of chitosan-coated 9 nm $MnFe_2O_4$ and 12 nm Fe_3O_4 were determined by the same method which was used for determining the relaxivity of water protons in the presence of $MnFe_2O_4$-Fe_3O_4 core-shell nanoparticles. $1/T_2$ vs. Fe concentration was plotted and r_2 (transverse relaxivity) was obtained by determining the slope of the line fitted to the data points. The plots used for the calculation of r_2 values are shown in Fig. 8.

Table 1 summarizes the values for the average size, saturation magnetization and transverse relaxivity obtained from the Fe_3O_4 nanoparticles, $MnFe_2O_4$ and $MnFe_2O_4$-Fe_3O_4 core-shell nanoparticles. It can be observed from table 1 that the highest value of the transverse relaxivity is obtained for the core-shell nanoparticles eventhough the saturation magnetization values and nanoparticle sizes are similar for the three cases. The highest value of transverse relaxivity in the case of core-shell nanoparticles illustrates that these nanoparticles created largest magnetic inhomogeneity in the water medium surrounding them. The origin of the greater

magnetic inhomogeneity was the difference in the magnetic nature of the $MnFe_2O_4$ and Fe_3O_4 phases in the core-shell nanoparticles.

To investigate the cytotoxicity of the $MnFe_2O_4$-Fe_3O_4 core-shell nanoparticles, MTT assay was performed using MCF-7 (human Brest cancer cells). Iron concentration of the chitosan coated nanoparticle dispersion was determined by AAS (Atomic Absorption Spectroscopy). The iron concentration of chitosan coated nanoparticles was determined by AAS. The standard solutions of 1, 2, 3, 4 and 5 ppm were prepared by using ferrous ammonium sulphate to obtain the calibration curve. 1 ml of nanoparticle dispersion, taken from the stock solution, containing chitosan coated core-shell nanoparticles were dissolved in 4 mL of concentrated H_2SO_4 contained in a 25 mL volumetric flask. Distill water was then added into the volumetric flask to fill it to 25 mL capacity. The absorbance value obtained for this solution was then used to determine the iron concentration in the stock solution using the calibration curve. Required volumes of the particle dispersion from the stock solution were then used for the MTT assay. Results from the cytotoxicity experiment shown in Fig. 9 clearly reveal that thecore shell nanoparticles with different concentrations (100, 50, 25, 12.5 and 6.25µg/mL) are bio-compatible towards the MCF-7 cell line.

4. Conclusions

This work illustrates the effect of ferrite-ferrite core-shell nanoparticle geometry on the enhancement in the proton relaxivity value using $MnFe_2O_4$-Fe_3O_4 core-shell nanoparticles as candidate material. For similar values of saturation magnetization and nanoparticle sizes, it was observed that the proton relaxivity value obtained in the dispersion of core-shell nanoparticles was considerably greater than the proton relaxivity value obtained in the presence of single phase nanoparticles of the core and shell phases. This highest value of transverse relaxivity in the case

core-shell nanoparticles was due to the largest magnetic inhomogeneity created by these nanoparticles. The origin of the greater magnetic inhomogeneity was the difference in the magnetic behaviour of the phases in the core and shell of the $MnFe_2O_4$-Fe_3O_4 core-shell nanoparticles.

5. Acknowledgement

Authors acknowledge the electron microscopy facilities available at the Advanced Centre for Microscopy and Microanalysis (AFMM) IISc Bangalore. The MCF-7 cell line were provided by Professor Paturu Kondaiah. Cell toxicity analysis was done using the facilities available in Professor Paturu Kondaiah's laboratory in IISc, Bangalore. C. Srivastava acknowledges the research grant received from Department of Science and Technology DST-Nano Mission and SERB, Govt. of India. The NMR facility at NMR Research Centre, supported by DST, is gratefully acknowledged.

References

1 R. G. Chaudhuri and S. Paria, *Chem. Rev.*, 2012, **112**, 2373–2433.

2 O. Masala, D. Hoffman, N. Sundaram, K. Page, T. Proffen, G. Lawes and R. Seshadri, *Solid State Sci.*, 2006, **8**, 1015–1022.

3 A. Burns, H. Ow and U. Wiesner, *Chem. Soc. Rev.*, 2006, **35**, 1028–1042.

4 K. Chatterjee, S. Sarkar, K. J. Rao and S. Paria, *Adv. Colloid Interface Sci.*, 2014, **209**, 8–39.

5 S. Sun and H. Zeng, *J. Am. Chem. Soc.*, 2002, **124**, 8204–8205.

6 T. Hyeon, *Chem. Commun.*, 2003, 927–934.

7 M. Green, *Small*, 2005, **1**, 684–686.

8 A. Lopez-Ortega, M. Estrader, G. Salazar-Alvarez, A. G. Roca and J. Nogues, *Phys. Rep.*, 2014, **553**, 1–32.

9 S. Manjura Hoque, C. Srivastava, V. Kumar, N. Venkatesh, H.N. Das, D.K. Saha and K. Chattopadhyay, *Mater. Res. Bull.*, 2013, **48**, 2871–2877.

10 J.-H. Lee, J. Jang, J. Choi, S. H. Moon, S. Noh, J. Kim, J.-G. Kim, I.-S. Kim, K. I. Park and J. Cheon, *Nat. Nanotechnol.*, 2011, **6**, 418–422.

11 Q. K. Ong, X.-M. Lin and A. Wei, *J. Phys. Chem. C Nanomater. Interfaces*, 2011, **115**, 2665–2672.

12 R. A. Vertree, A. Leeth, M. Girouard, J. D. Roach and J. B. Zwischenberger, *Perfusion*, 2002, **17**, 279–290.

13 P. Wust, B. Hildebrandt, G. Sreenivasa, B. Rau, J. Gellermann, H. Riess, R. Felix and P. Schlag, *Lancet Oncol.*, 2002, **3**, 487–497.

14 R. R. Edelman and S. Warach, *N. Engl. J. Med.*, 1993, **328**, 708–716.

15 A. S. Merbach, L. Helm and E. Toth, *The Chemistry of Contrast Agents in Medical Magnetic Resonance Imaging*, John Wiley & Sons, 2013.

16 H. B. Na, I. C. Song and T. Hyeon, *Adv. Mater.*, 2009, **21**, 2133–2148.

17 C. Sun, J. S. H. Lee and M. Zhang, *Adv. Drug Deliv. Rev.*, 2008, **60**, 1252–1265.

18 P. Chhour, N. Gallo, R. Cheheltani, D. Williams, A. Al-Zaki, T. Paik, J. L. Nichol, Z. Tian, P. C. Naha, W. R. Witschey, H. R. Allcock, C. B. Murray, A. Tsourkas, and D. P. Cormode, *ACS Nano*, 2014, **8(9)**, 9143-9153.

19 P. C. Naha, A. A. Zaki, E. Hecht, M. Chorny, P. Chhour, E. Blankemeyer, D. M. Yates, W. R. Witschey, H. I. Litt, A. Tsourkas, D. P. Cormode, *J. Mater. Chem. B: Mater. Bio. Med.*, 2014, **2(46)**, 8239-8248.

20 N. Teraphongphom, P. Chhour, J. R. Eisenbrey, P. C. Naha, W. R. Witschey, B. Opasanont, L. Jablonowski, D. P. Cormode, M. A. Wheatley, Langmuir, 2015, **31(43)**, 11858-11867.

21 H. Yang, C. Zhang, X. Shi, H. Hu, X. Du, Y. Fang, Y. Ma, H. Wu, S. Yang, *Biomaterials,* 2010, **31**, 3667-3673.

22 U. I. Tromsdorf, N. C. Bigall, M. G. Kaul, O. T. Bruns, M. S. Nikolic, B. Mollwitz, R. A. Sperling, R. Reimer, H. Hohenberg, W. J. Parak, S. Fo1rster, U. Beisiegel, G. Adam, H. Weller, *Nano Lett.*, 2007, **7(8)**, 2422-2427.

23 H. Khurshid, C.G. Hadjipanayis , H. Chen , W. Li, H. Mao, R. Machaidze, V. Tzitzios and G. C. Hadjipanayis, *J. Magn. Magn. Mater.*, 2013, **331**, 17–20.

24 S. Laurent, D. Forge, M. Port, A. Roch, C. Robic, L. V. Elst and R. N. Muller, *Chem. Rev.*, 2008,**108**, 2064–2110.

25 A. Lopez-Cruz, C. Barrera, V. L. Calero-Ddelc and C. Rinaldi, *J. Mater. Chem.*, 2009, **19**, 6870-6876.

26 M. Zhang, X. H. Li, Y. D. Gong, N. M. Zhao and X. F. Zhang, *Biomaterials*, 2002, **23**, 2641–2648.

27 H. Gunther, *NMR Spectroscopy: Basic Principles, Concepts and Applications in Chemistry*, John Wiley & Sons, 2013.

28 P.C. Naha, M. Davoren, F. M. Lyng, H. J. Byrne, *Toxicol Appl Pharmacol.*, 2010, **246(1-2)**, 91-99.

29 J. Cao, W. Fu, H. Yang, Q. Yu, Y. Zhang, S. Liu, P. Sun, X. Zhou, Y. Leng, S. Wang, B. Liu and G. Zou, *J. Phys. Chem. B*, 2009, **113**, 4642–4647.

30 A. L. Patterson, Phys. Rev., 1939, **56**, 978-982.

31 Z. Li, S. X. Wang, Q. Sun, H. L. Zhao, H. Lei, M. B. Lan, Z. X. Cheng, X. L. Wang, S. X.

Dou and G. Q. Lu, *Adv. Healthc. Mater.*, 2013, **2**, 958–964.

32 Q. K. Ong, X.-M. Lin and A. Wei, *J. Phys. Chem. C Nanomater. Interfaces*, 2011, **115**, 2665–2672.

33 C. Constantinides, *Magnetic Resonance Imaging the Basics*, CRC Press, Boca Raton, 2014.

34 N. A. Frey, S. Peng, K. Cheng and S. Sun, *Chem. Soc. Rev.*, 2009, **38**, 2532–2542.

Table Caption

Table 1: List of average particle size, saturation magnetization and transverse relaxivity values.

Figure captions:

Fig. 1 XRD profiles obtained from the $MnFe_2O_4$ seeds and $MnFe_2O_4$-Fe_3O_4 core-shell nanoparticles.

Fig. 2 (a) TEM bright field image and SAD pattern obtained from $MnFe_2O_4$ seed nanoparticles, (b) Size distribution histogram of $MnFe_2O_4$ seed nanoparticles, (c) TEM bright field image and SAD pattern obtained from $MnFe_2O_4$-Fe_3O_4 core-shell nanoparticles, (d) Size distribution histogram of core-shell nanoparticles, (e) STEM-HAADF image of core shell nanoparticles and (f) EDS compositional profile obtained for Mn along line the A-B (from Fig. 2(e)). The red box in the image 2(e) is the reference use for the drift correction routine during the EDS measurement.

Fig. 3 XPS spectrums showing (a) Mn, (b) Fe (c) O peaks and (d) full XPS spectrum of $MnFe_2O_4$ seeds and $MnFe_2O_4$-Fe_3O_4 core-shell nanoparticles.

Fig. 4 (a) M-H curves obtained from $MnFe_2O_4$ seeds and $MnFe_2O_4$-Fe_3O_4 core-shell nanoparticles and (b) zero field cooled (ZFC) curves obtained from seeds and core-shell nanoparticles.

Fig. 5 (a) Decay curves for different iron concentrations obtained for water protons in the presence of chitosan coated core shell nanoparticles, **(b)** $1/T_2$ vs. Fe concentration curve of water protons in the presence of chitosan coated $MnFe_2O_4$-Fe_3O_4 core-shell nanoparticles.

Fig. 6 (a) XRD profile, (b) TEM bright field image and SAD pattern (c) Size distribution histogram and (d) M vs. H curve obtained from 9 nm $MnFe_2O_4$ nanoparticles.

Fig. 7 (a) XRD profile, (b) TEM bright field image and SAD pattern (c) Size distribution histogram and (d) M vs. H curve obtained from 12 nm Fe_3O_4 nanoparticles.

Fig. 8 $1/T_2$ vs. Fe concentration curves of water protons in the presence of chitosan coated (a) 9 nm $MnFe_2O_4$ and (b) 12 nm Fe_3O_4 nanoparticles.

Fig. 9 MTT assay of chitosan coated $MnFe_2O_4$-Fe_3O_4 core shell nanoparticles. Incubation time was 24 hours.

Sample	Average Size (nm)	Saturation Magnetization (emu/g)	Transverse relaxivity ($mM^{-1}s^{-1}$)
$MnFe_2O_4$	9	61.5	83.2
Fe_3O_4	12	65.8	96.6
$MnFe_2O_4$-Fe_3O_4 core-shell	12.5	69.34	184.1

Table 1 List of average particle size, saturation magnetization and transverse relaxivity values.

Figure 1.

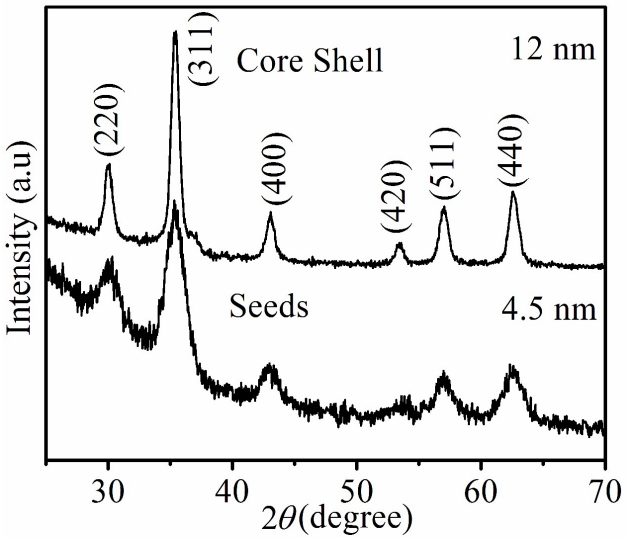

Figure 2.

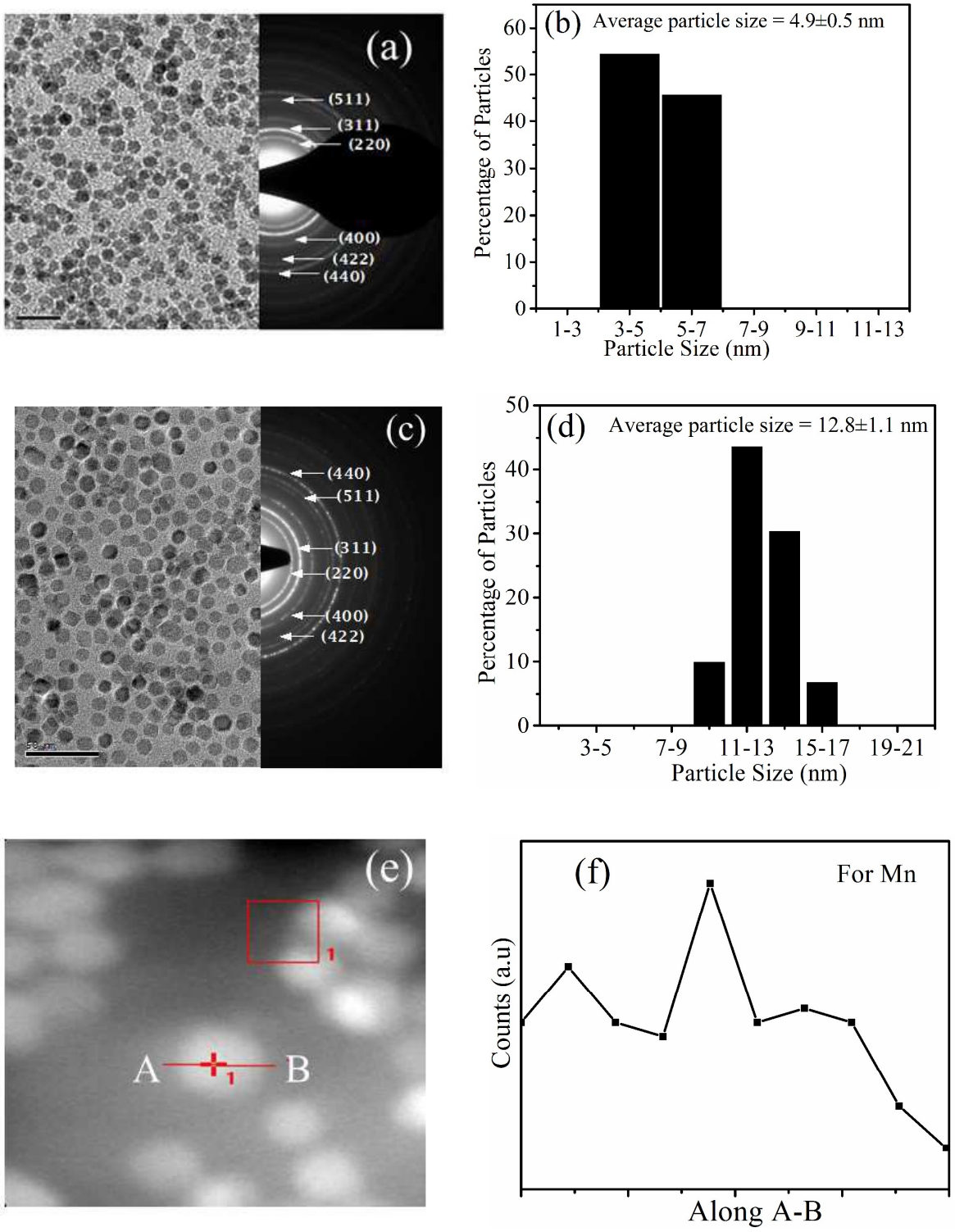

Figure 3.

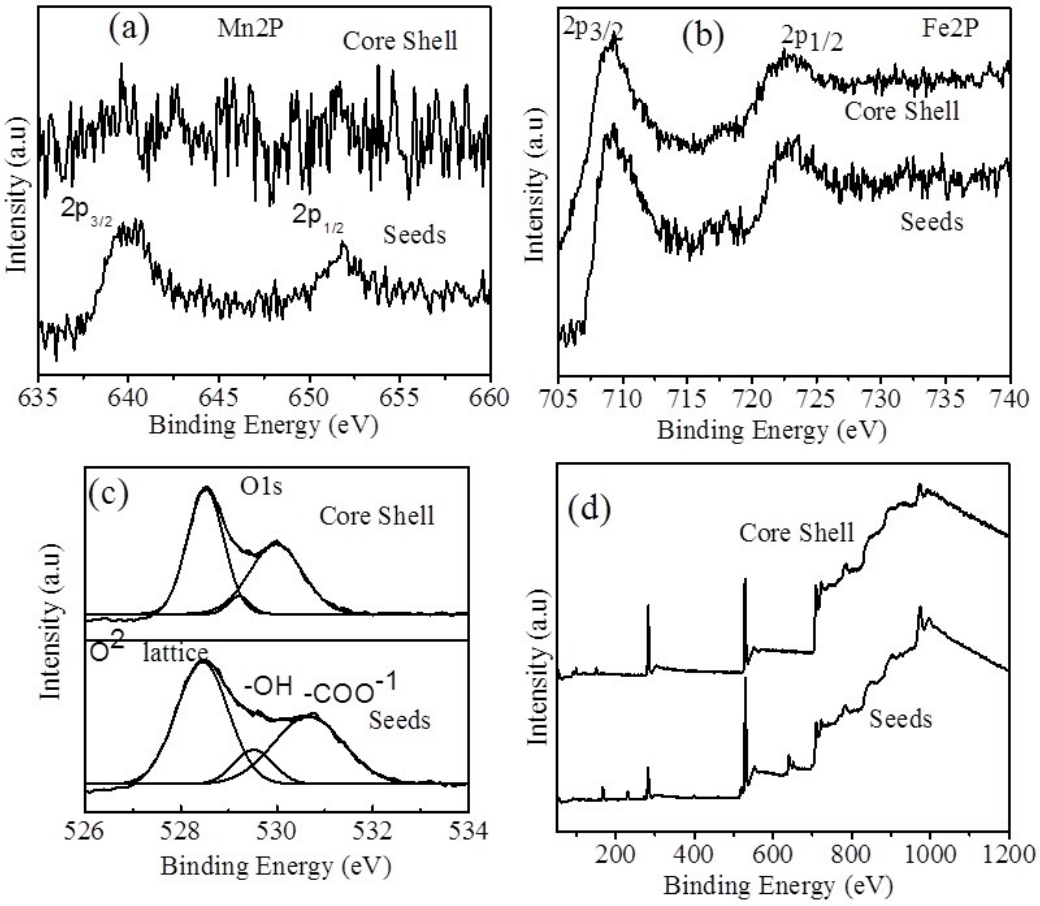

Figure 4.

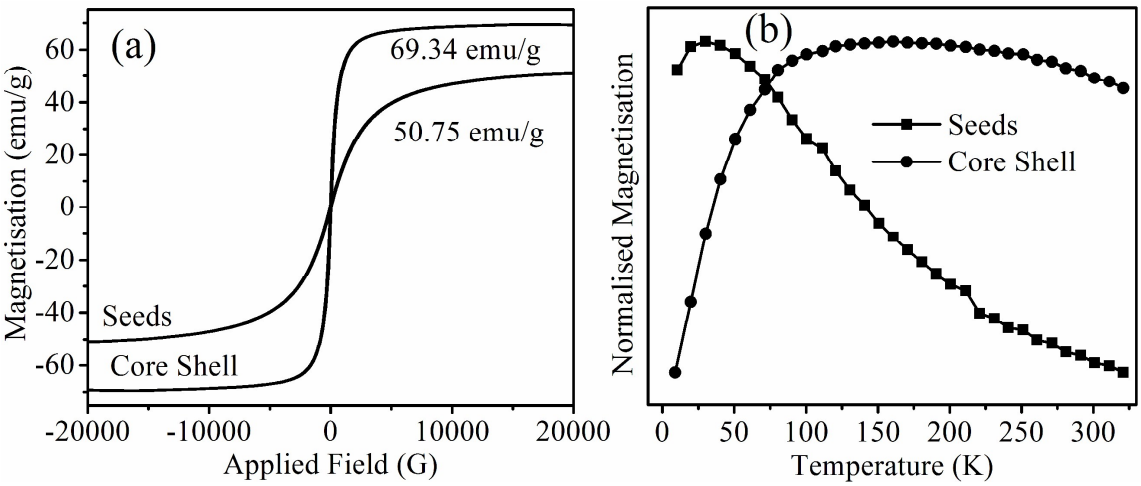

Figure 5.

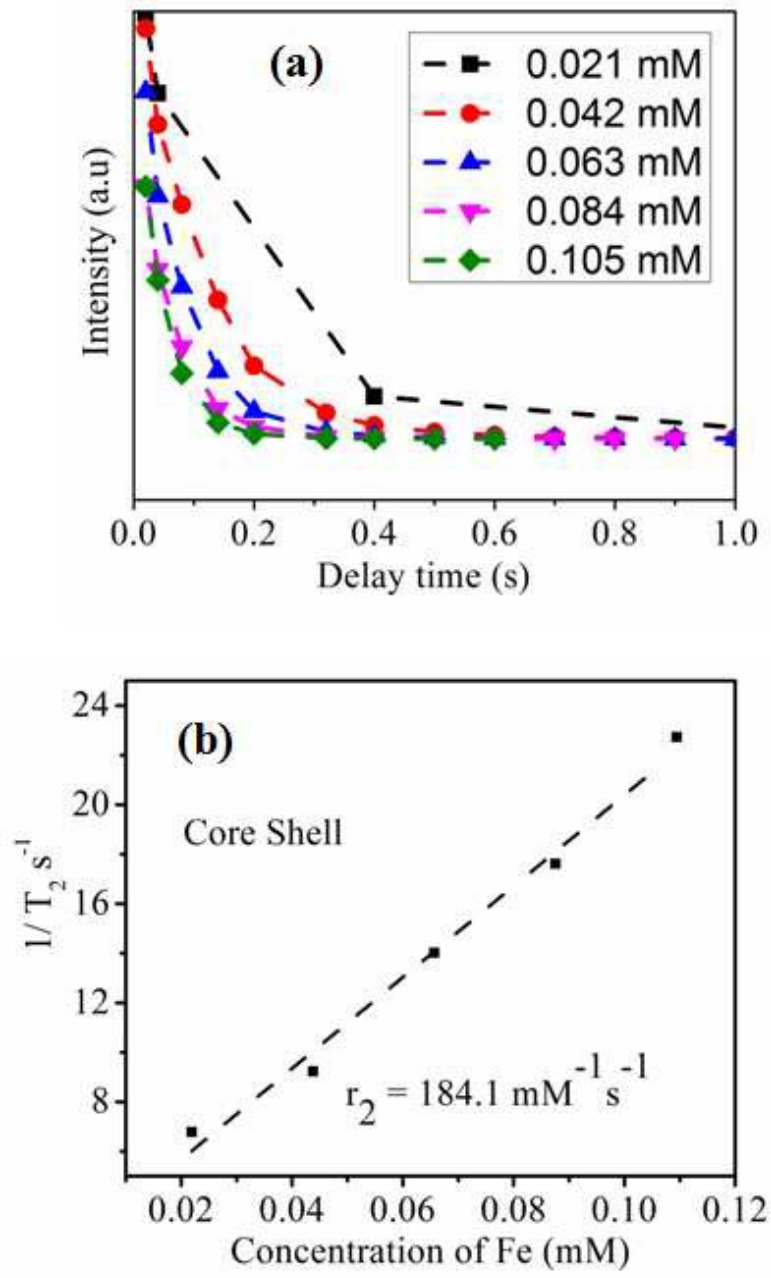

Figure 6.

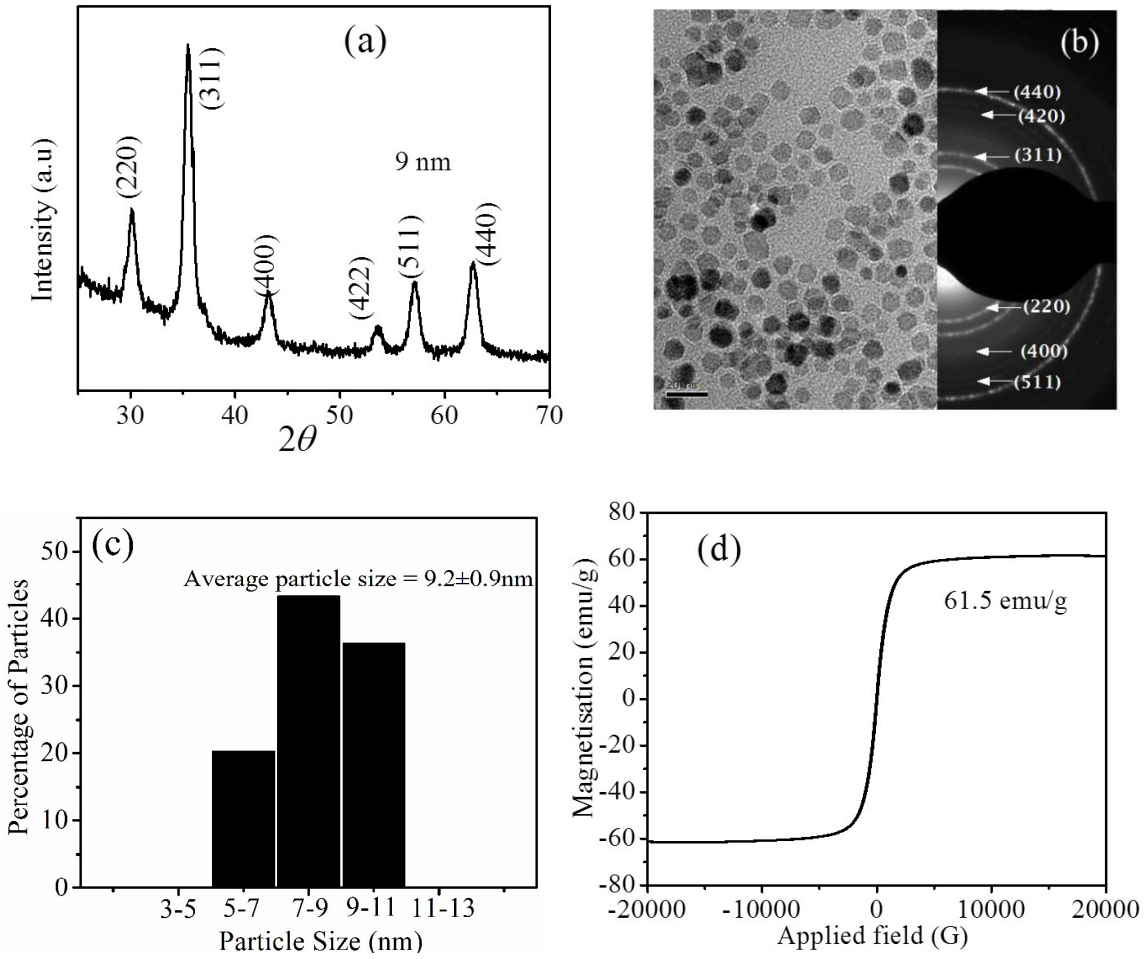

Figure 7.

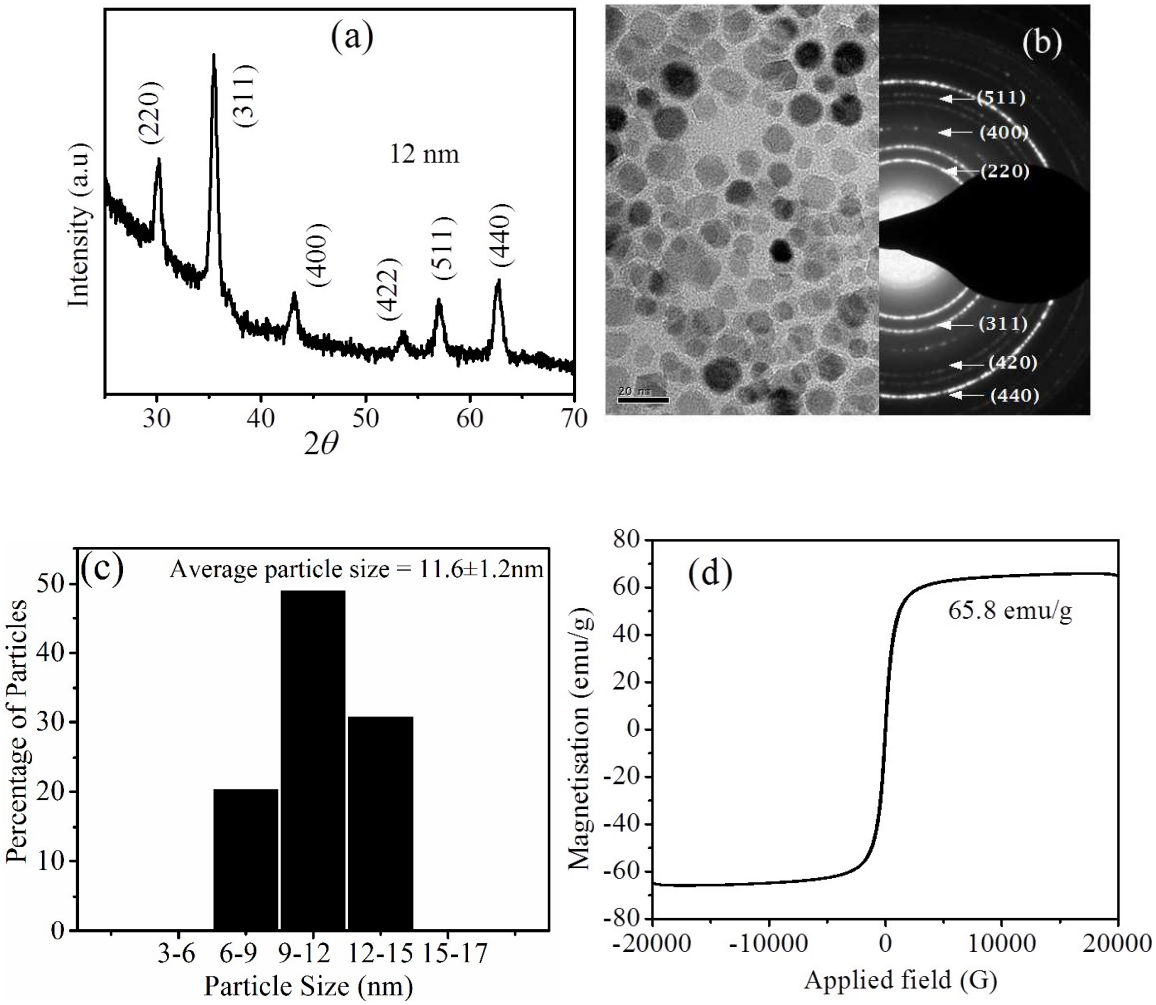

Figure 8.

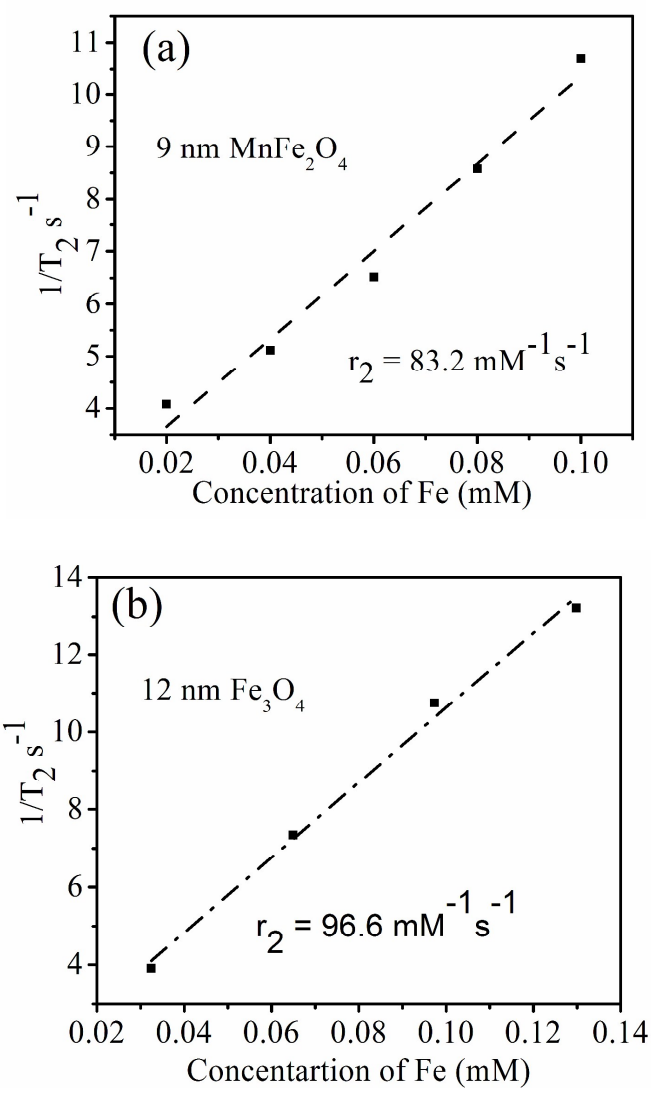

Figure 9.